minerals

MDPI

Article

Low-Temperature Thermochronology Records the Convergence between the Anatolide–Tauride Block and the Arabian Platform along the Southeast Anatolian Orogenic Belt

Semih Gildir [1], Fatih Karaoğlan [1,2,*] and Erhan Gülyüz [3,4]

[1] Geological Engineering Department, Engineering Faculty, Çukurova University, 01330 Adana, Türkiye; smhgldr@gmail.com
[2] Department of Geological Processes, Institute of Geology of the Czech Academy of Sciences, 16500 Prague, Czech Republic
[3] Mühendislik Fakültesi, Jeoloji Mühendisliği Bölümü, Van Yüzüncü Yıl Üniversitesi, 65080 Van, Türkiye; erhangulyuz@yyu.edu.tr
[4] Department of Neotectonics and Thermochronology, Institute of Rock Structure and Mechanics of the Czech Academy of Sciences, 18209 Prague, Czech Republic
* Correspondence: fkaraoglan@cu.edu.tr

Abstract: SE Anatolia is witnessing the final stage of the Wilson Cycle, where a continental collision between the Tauride–Anatolide block and Arabian platform occurred, and a 1.5 km Eastern Tauride mountain chain formed. We present new low-temperature thermochronology (LTT) ages, including eight apatite fission track (AFT) and seven apatite and zircon U-Th-Sm/He (AHe, ZHe) ages, for the metamorphic rocks from the Nappe Zone of the Southeast Anatolian Orogenic Belt. The ZHe ages vary from 51.2 ± 0.7 Ma to 30.4 ± 0.6 Ma, the AFT ages range from 33.1 ± 1.6 Ma to 18.1 ± 0.9 Ma, and the AHe ages range from 23.6 ± 2.5 Ma to 6 ± 1.9 Ma. The LTT data show a continuous slow uplift of the region. However, the thermal modeling results suggest an Eocene and middle–late Miocene fast uplift of the region. Similar to our results, the LTT studies along the SAOB show that the vertical movements initiated during the Eocene period have continued in a steady-state regime to recent times. The Eocene epoch is identified by arc–back-arc setting in the region, whereas the Miocene epoch is marked by the continental collision. Within this tectonic framework, vertical movements on the overriding plate are controlled by both extensional and compressional tectonics. The LTT data obtained along the SAOB show fingerprints of thrust propagation from north to south.

Keywords: SE Anatolia; low-temperature thermochronology; thrust propagation; uplift

check for updates

Citation: Gildir, S.; Karaoğlan, F.; Gülyüz, E. Low-Temperature Thermochronology Records the Convergence between the Anatolide–Tauride Block and the Arabian Platform along the Southeast Anatolian Orogenic Belt. *Minerals* **2024**, *14*, 614. https://doi.org/10.3390/min14060614

Academic Editors: Ruxin Ding, Honghua Lv and Rong Yang

Received: 17 May 2024
Revised: 10 June 2024
Accepted: 12 June 2024
Published: 15 June 2024

Copyright: © 2024 by the authors. Licensee MDPI, Basel, Switzerland. This article is an open access article distributed under the terms and conditions of the Creative Commons Attribution (CC BY) license (https://creativecommons.org/licenses/by/4.0/).

1. Introduction

The convergence of continents fundamentally involves the subduction of oceanic crust, leading to the collision of converging continental masses and the eventual ocean closure between the continents. It encompasses a myriad of complex phenomena, influenced by factors such as the subduction rate of the descending slab; the presence of seamounts or continental fragments within the convergence system; and the rollback, tearing, or detachment of the subducting slab in the later stages of subduction. Since these convergence processes occur over long geological periods and involve interactions between the subducting oceanic crust (and latterly the continental crust?) and the converging continental blocks, the recorded vertical movement, rate, and geothermal gradient at each moment and location exhibit heterogeneous behavior. This variability leads to the formation of mountain ranges, high plateaus, or depression areas at different times and locations within the convergent system. Thermal models based on low-temperature thermochronology (LTT), which aim to understand the time-dependent vertical (cooling) movements at different points within a convergent system, provide powerful quantitative datasets for analyzing the temporal and spatial evolution of such systems. In this context, the tectonic position of the LTT

data collection point, the type of sampled units (magmatic, metamorphic, sedimentary, etc.), and the last-recorded high-temperature (i.e., >200 °C) age at the sample location are critically important for interpreting the thermal/uplift/exhumation evolution of the point. Consequently, these factors are essential for understanding the evolution of the convergence process that caused the thermal events affecting the sample point.

To understand the timing and upper-crustal effects of the convergence events between the Arabian and Eurasian plates, the Permian Yoncayolu Formation in eastern Anatolia has been sampled for low-temperature thermochronology. The deposition age of the Permian Yoncayolu Formation coincides with the opening of the Neotethys Ocean. However, this unit later moved along with a continental fragment located on the northern edge of the opening ocean. It subsequently experienced subduction-related blueschist metamorphism during the Cretaceous–Paleocene period, following the complete consumption of the Berit Ocean's subducting oceanic crust beneath the Eurasian plate to its north [1–4]. The main uplift/exhumation/cooling events experienced by the unit after the subduction-related metamorphism are expected to be associated with the ongoing convergence events between the main Arabian plate, located on the southern margin of the Neotethys Ocean that began opening in the Permian, and the Eurasian continent, which had amalgamated with fragments of the Arabian plate located on the northern margin of the ocean.

In this context, the Southeast Anatolian Orogenic Belt (SAOB) can be defined as a regional-scale tectonic belt that demonstrates the characteristics of a complete Wilson Cycle, including (i) rifting during the Permo–Triassic, (ii) the development of an oceanic environment extending over a width of 600 km [5,6], (iii) the subduction and demise of oceanic crust, (iv) the growth of an imbrication zone and arc crust, and (v) continental collisions from the late Cretaceous to recent times [1,2,7–10].

In this picture, three different major tectonic units are defined for the SAOB, namely the Malatya–Keban–Binboğa metamorphics (MKB) to the north, the Bitlis–Pütürge–Engizek (BPE) metamorphics in the middle, and the Arabian platform to the south, which once formed the northern margin of the Gondwana (Figure 1) [4,11–13]. The Berit Ocean was located in the north, separating the MKB and BTE, whereas the southern branch of the Neotethyan Ocean was located in the south, separating the Arabian platform and the BTE. The collision of the MKB (eastern Taurides) and the BTE occurred during the late Cretaceous, which led to the juxtaposition of these two continental crusts. The BTE experienced blueschist metamorphism during the subduction beneath the eastern Taurides in a north-dipping setting, and were exhumed during the late Cretaceous–Paleocene at some depths of 6–8 km [1,2,14,15]. After this period, the BPE became the southern margin of the eastern Taurides and was the active margin, whereas the southern branch of the Neotethyan Ocean was consumed in a north-dipping subduction setting.

The post-Paleocene convergence events for the study area are supported by numerous studies, indicating their significant role in (i) the formation of Eocene–Miocene arc magmatism [16–19], (ii) the termination of the connection between the Indian Ocean and the Mediterranean Sea approximately 20 million years ago [7,20–23], (iii) the formation of the Eastern Anatolian high plateau (with an average elevation of 1.5 km) [21] and the formation of the Bitlis–Zagros orogenic belt [7,15,18,24–26], and (iv) the collision along the SAOB that continues and deforms the crust, forming the neotectonics and active tectonic structures for the whole of Anatolia [27–34]. The westward escape of the Anatolian plate was facilitated by the formation of the North Anatolian and East Anatolian fault zones [27,28,35,36].

In this context, the post-Paleocene convergence in the region could have led to uplift/exhumation events during the period when ongoing subduction experienced slab rollback, potentially resulting in an extensional exhumation in the back-arc or fore-arc depression areas of the active margin. As convergence continued, the continents amalgamated, causing the entire region to experience compressional regime effects and uplift. During these amalgamation events, the propagation of nappe stacks could be expected to move towards the subducting continent, similar to what is observed in the Himalayas (i.e., Li et al. [37]). However, to date, low-temperature thermochronology (LTT) studies

conducted in the region have not been able to distinguish between the periods of subduction (potentially an extensional period) and collision (potentially a compressional period). Additionally, these studies have been insufficient for determining the pace and mode of nappe stack movements.

In this regard, this study aims to develop high-resolution exhumation/uplift models for a setting characterized by multiple tectonic events, specifically for the active margin where upper-crustal scale exhumation has occurred during the post-Paleocene period. The primary aim is to determine which of the aforementioned major tectonic events can be traced through high-resolution thermal models fed by zircon U-Th-Sm/He (ZHe), apatite fission track (AFT), and apatite U-Th-Sm/He (AHe) data, and to better constrain the timing of these events with new datasets.

Geological Setting

The Southeast Anatolian Orogenic Belt was formed by three major tectonic units separated by sutures, from south to north: the Arabian plate, the accretionary zone, and the Nappe Zone (Figure 1) [18]. The Bitlis, Pütürge, and Engizek metamorphics (BPE) formed the lower metamorphic units. They were located between the Arabian platform to the south and the Anatolide–Tauride platform to the north during the late Cretaceous [4,11,38].

The study area is located north of Kahramanmaraş city, SE Turkey, and comprises Cretaceous and older rocks, including metamorphic and magmatic rocks. The basement rocks are represented by late Paleozoic–Triassic-aged Engizek metamorphics, comprising phyllite, mica gneiss, mica schists, metasandstone, quartz schist, amphibolite, amphibole schist, marble, and calcschist. A meta-granite intruded into these rock associations in the region. These units are thrusted over by Jurassic–Lower Cretaceous carbonate rocks [39]. These rocks are overlain by early–late Cretaceous-aged turbiditic limestones intercalated with sandstone, shale, claystone, cherty limestone, limestone volcano–sedimentary rocks, and serpentinite. An ophiolitic mélange, including serpentinite, peridotite, gabbro, diabase, and volcanic olistostrome with limestone blocks, tectonically overlies these units. To the west of the study area, an ophiolitic sequence (Göksun ophiolite) intruded by the granitoid body Esence Granitoid tectonically overlies all these units. The middle Eocene-aged Maden mélange and Neogene units conformably overlie all the units in the region (Figures 1 and 2) [39–41].

The Yoncayolu formation is exposed in the Engizek metamorphics, part of the Nappe Zone of the SAOB. The unit consists of phyllite, mica gneiss, mica schists, metasandstone, quartz schist, amphibolite, amphibole schist, marble, and calcschist, and regarding the fossil content of the unmetamorphosed parts of the unit, a pre-Permian–Permian age has been assigned to the unit by previous studies [41] (Figures 1 and 2). The unit overlies the Göksun ophiolite in the study area and is tectonically overlain by the Permian Çayderesi formation (Figures 1 and 2) [39,41,42]. The active Sürgü–Çardak fault, which produced one of the biggest earthquakes (M: 7.8; 6 February 2023) in Turkey during the instrumental period, bounds the northern margin of the Yoncayolu formation.

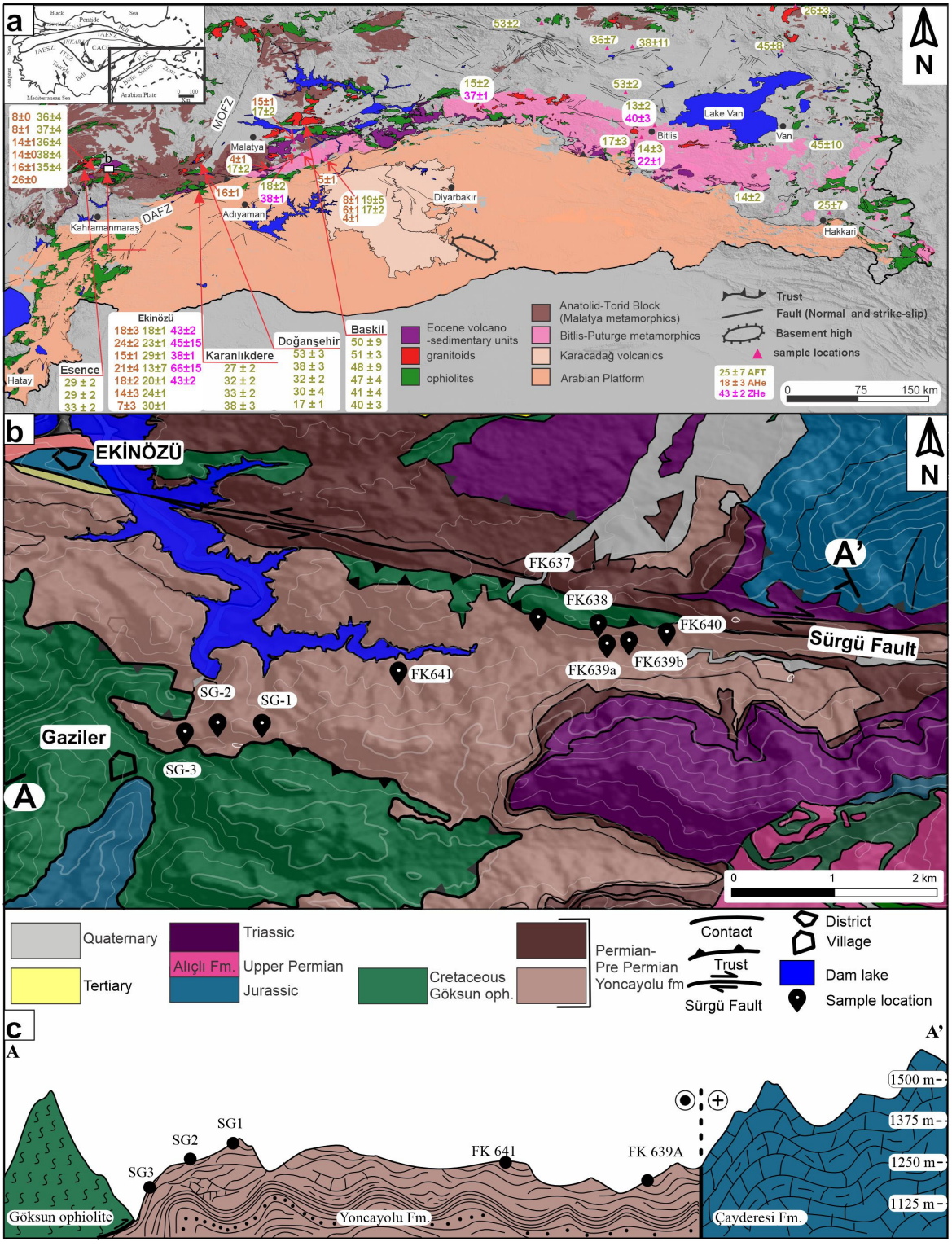

Figure 1. (**a**) Generalized geological map of the Southeast Anatolian Orogenic Belt, SE Turkey. The inset map shows the major tectonic units of Anatolia [18,43–48]. The numbers show the LTT data along the SAOB. The LTT data are from Okay, Zattin, and Cavazza [7]; Karaoğlan, Parlak, Hejl, Neubauer, and Klötzli [11]; Cavazza, Cattò, Zattin, Okay, and Reiners [15]; Topak [25]; and Whitney, Delph, Thomson, Beck, Brocard, Cosca, Darin, Kaymakcı, Meijers, Okay, Rojay, Teyssier, and Umhoefer [34]. (**b**) Geological map of the study area, including the sampling sites. The map is modified from Hozatlıoğlu, Bozkaya, and Yalçın [39]. A-A': cross-section in Figure 1c, (**c**) Cross-section showing the sampling points.

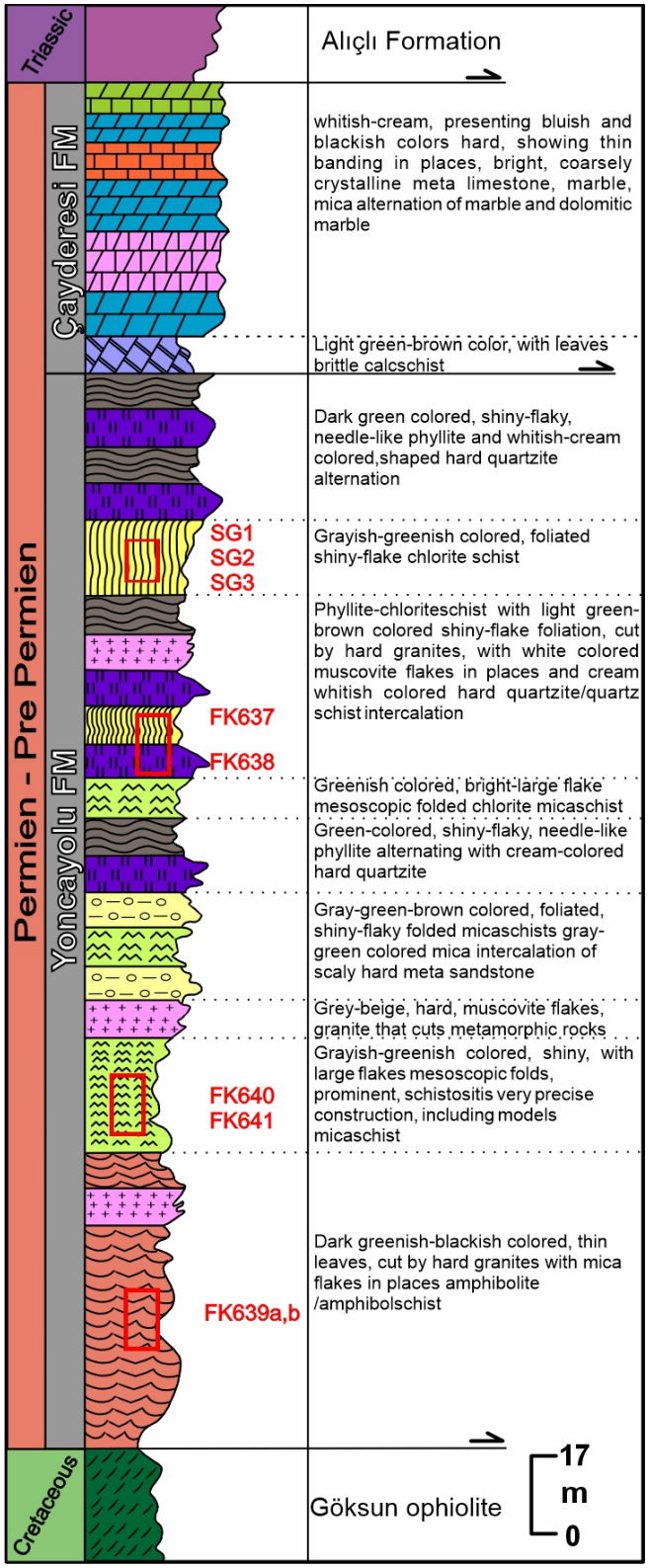

Figure 2. Stratigraphic columnar section of the Ekinözü region [39]. The red boxes show the sample locations within the section. Note that the Yoncayolu formation trusts Göksun ophiolite; however, in the study area, it is vice versa due to the nappe piles.

2. Materials and Methods

Nine samples were collected from the Yoncayolu formation for applying LTT and zircon U-Pb analyses (Table 1, Figures 1–3). All the samples were collected to the south of the Sürgü fault zone, where the Yoncayolu formation outcropped. All the samples showed schistosity in the field (Figure 3a–j). Samples FK637, FK638, FK639a,b, FK640, and FK641 were collected at the same elevation in the Nergile Valley, south of Ekinözü county, Figures 1, 2 and 3a–j). Samples SG1, SG2, and SG3 were collected on a ridge to test the age–elevation relation (Table 1). The petrographic thin sections were prepared at the laboratories of the Geological Engineering Department of Cukurova University (Adana, Turkey).

Table 1. Samples collected for LTT and zircon U-Pb analyses (see Supplementary File S1 for petrographic description).

Sample	Lithology	Lat	Long	Altitude (m)
FK637	mica–quartz schist	38.021438	37.17277	1180
FK638	muscovite schist	38.019075	37.1873	1181
FK639a	amphibole schist	38.017914	37.18866	1180
FK639b	mica–quartz schist	38.017914	37.18866	1180
FK640	mica–quartz schist	38.018566	37.19313	1185
FK641	mica–quartz schist	38.092591	37.14769	1157
SG-1	plg + bio + quartz schist	38.00113	37.12302	1275
SG-2	bio + chlorite schist	38.001756	37.11594	1190
SG-3	bio + plg + quartz schist	38.000647	37.11036	1130

The zircon U-Pb analyses were performed at the Geology Institute of the Czech Academy of Sciences (Prague) using a Teledyne Cetac excimer laser with a HelEx II 2-Volume sample chamber attached to a Thermo Scientific™ Element XR™ HR-ICP-MS. Žák et al. [49] presented detailed analytical conditions for zircon U-Pb analyses, which are also presented in Supplementary File S1.

The laser ablation fission track (LAFT) method was used for the AFT analyses. The track counting, Dpar, and confined track length (TL) measurements were carried out by an XYZ motorized stage attached to a Nikon LV100ND microscope in the laboratories of the Geological Engineering Department of Cukurova University. The ^{238}U concentration was measured by an ESI NWR213 attached to a Perkin Elmer Nexion 2000P quadrupole ICP-MS at the Central Research Laboratory (CUMERLAB) of Cukurova University (Adana, Turkey). Readers may refer to Gulyuz [50] for the detailed methodology, which is also presented in Supplementary File S1.

The apatite and zircon U-Th/He analyses were performed at the Institute of Rock Structure and Mechanics of the Czech Academy of Sciences, Prague (Czech Republic). Three to five grains were analyzed for each sample. Euhedral, optically fluid/mineral inclusion-free zircon and apatite grains (length and width of >60 μm) were handpicked under a binocular microscope. The dimensions of the selected grains were measured and recorded, and their photomicrographs were taken in two different orientations to calculate the α-ejection corrections (FT) factors [51,52] for the age calculations. A fully automated Alphachron© He extraction instrument was used for measuring the ^{4}He concentrations. To validate the measurements, Durango and Fish Canyon Tuff apatites were used during the measurements. Durango apatite was used as the analytical standard to check the analytical accuracy of the AHe ages, whereas Fish Canyon Tuff zircon was used for the ZHe ages. After degassing, the grains were dissolved in concentrated HNO_3 and HF acidic solutions and spiked with standards containing known quantities of U, Th, and Sm. The ^{238}U, ^{235}U, ^{232}Th, and ^{147}Sm concentrations of each dissolved grain were measured using a Thermo Fisher Scientific ELEMENT 2 HR-ICP-MS at the Institute of Geology of the Czech Academy

of Sciences. The age of each grain was calculated using the standard radioactive decay equation, standardized by Farley [51], and the calculated ages were corrected by FT to obtain the corrected ages [51,52].

Figure 3. Field photos of the samples. (**a**–**i**) General and close views of the samples; (**j**) general view of the Nergile valley, showing the active Sürgü fault and sample locations. Msg: Göksun ophiolite.

The thermal history models were calculated using QTQt (v5.8.0) for each sample, using inverse modeling based on the Bayesian trans-dimensional Markov Chain Monte Carlo (MCMC) statistical method [53]. The single grain age data, confined track length data with c-axis, Dpar values, and ZHe and AHe data were used as the input values to reveal the cooling histories of the samples through the apatite PAZ and AHe partial retention zone (APRZ) [53]. The published Ar-Ar ages (350 °C at 45 ± 1 Ma) [39] of the Yoncayolu formation and the zircon U-Pb ages (700 °C at 60 ± 2 Ma) from this study were used as the geological constraints. The MCMC runs 250,000 burn-in and 250,000 post-burn-in iterations, whereas the annealing model of Ketcham et al. [54], the apatite radiation damage accumulation and annealing model (RDAAM) of Flowers et al. [55], and the zircon radiation damage accumulation and annealing model (ZRDAAM) of Guenthner

et al. [56] with default spherical grain geometry were used for thermal history modeling. QTQt requires the uncorrected ages as the input for alpha ejection and calculates the He ejection during the modeling process following Ketcham et al.'s [57] equations.

3. Results

3.1. Zircon U-Pb Dating

Four samples were subjected to LA-ICP-MS zircon U-Pb analyses to better determine the source of the metamorphic rocks (Figure 4). Since the four samples belonged to the same unit, 20 grains were analyzed from each sample (FK641 had only 11 grains), and all the results were combined into one group.

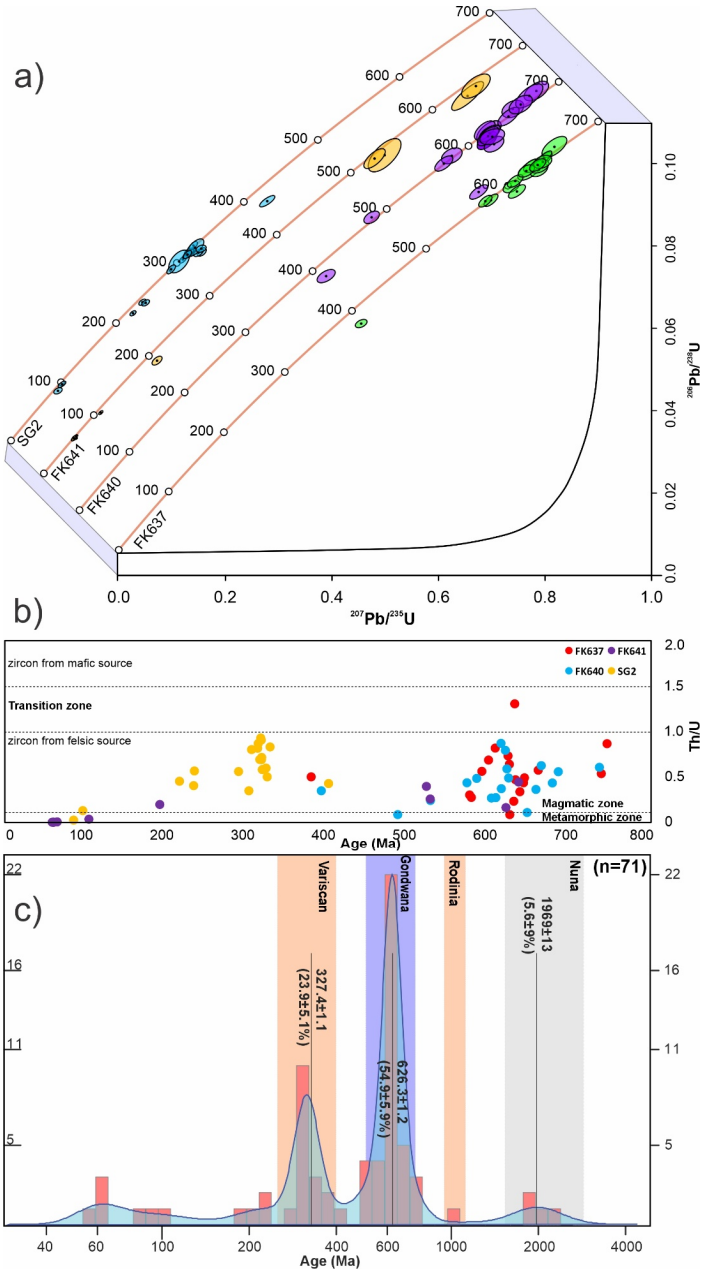

Figure 4. (**a**) Stacked Concordia diagrams of all samples; (**b**) Th/U ratio vs. age diagram for all samples [51]; (**c**) zircon U-Pb age histogram of all grains [58,59]. Note that in (**a**) and (**b**), 5 grains (ages > 1000 Ma) were not plotted to emphasize the distribution of the majority of the grains.

The CL images show mostly oscillatory zoning, indicating a magmatic origin; however, some grains show patchy zoning, indicating a metamorphic origin. The zircon grains have either euhedral-shaped or rounded shards with a 1:1 to 1:3 length/width ratio (Supplementary File S1, Figures S2–S5). The outermost rims show metamorphic growth (<1 µm) (Supplementary File S1, Figures S2–S5). However, these parts were unable to be measured by LA-ICP-MS. Twenty grains were analyzed, and all provided concordant ages (90–105%) (Supplementary File S2). The U-Pb ages ranged between 380 and 2190 Ma, whereas the Th/U ratios ranged between 0.1 and 3.4 (Supplementary File S2, Table S1, Figure 4).

The zircon U-Pb data show that two major sources fed the Yoncayolu formation. The zircons with Gondwana affinity are the primary source, and Variscan magmatism is the second source. However, there are zircons with ages clustered around 220 Ma (6%), 95 Ma (5%), and 60 Ma (6%). Those in the age clusters of 60 Ma and 95 Ma have Th/U ratios ranging between 0.00 and 0.04 (except for one, which is 0.13), indicating a metamorphic origin. However, the zircons in the 220 Ma cluster have Th/U ratios ranging between 0.2 and 0.57, indicating a felsic magmatic source (Figure 4, Supplementary File S2). A Devonian–Permian age has been assigned to the Yoncayolu formation based on the fossil content; however, the formation age of the unit may be late Triassic according to our zircon U-Pb data. The 60 Ma metamorphic zircon cluster is consistent with the regional metamorphism dated within the Bitlis–Pütürge metamorphics [1,2].

3.2. Apatite Fission Track Dating

A summary of the AFT analyses is given in Table 2, and radial plots are presented in the Supplementary File S1 Figure S6. The AFT central ages range from 18.1 ± 0.9 to 33.1 ± 1.6 Ma (Table 2). All the ages are significantly younger than either the formation or the defined metamorphism ages, indicating a cooling event related to exhumation. The altitudes of samples FK637, FK638, FK639b, FK640, and FK641 are similar. However, the AFT ages show dispersion, indicating that the Yoncayolu formation was shaped after exhumation. Samples SG1, SG2, and SG3 were collected on a ridge to test the altitude–age relation. However, the analytical data quality was not good due to the grain numbers and grain quality; the ages become younger from top to bottom, indicating a single-phase exhumation. SG1 passed the P(χ2) test (<0.05), whereas SG2 and SG3 failed the P(χ2) test (<0.05), indicating multiple populations; however, these samples should be interpreted with caution due to the number of analyzed grains. The rest of the samples passed the P(χ2) test (>0.05), indicating a single population. Three samples yielded sufficient track length (TL) measurements, but we used the TL measurements of FK640 and FK641. The mean track length (MTL) values of the samples FK637, FK638, FK639b, FK640, and FK641 are similar to each other and range between 10.61 and 11.57, with standard deviations ranging from 1.92 to 2.29, with an unimodal distribution indicating a slow cooling within the Partial Annealing Zone (PAZ) (Table 3).

Table 2. Summary table of apatite fission track analytical data for metamorphic rocks. N_s: number of spontaneous tracks counted; ρ_s: spontaneous track density; ^{238}U: average uranium concentration; N_L: number of confined track lengths measured; MTL: mean confined track length; SD: standard deviation of the track length distribution; Dpar: mean track etch pit diameter parallel to the crystallographic c-axis; Durango: standard apatite.

Sample Number	No. of Grains	N_s	ρ_s (10^5 cm^{-2})	^{238}U (µg/g)	Dpar (µm)	P(χ2)	Pooled Age (Ma ± 1σ)	Central Age (Ma ± 1σ)	N_L	MTL (µm)	SD (µm)
FK637	33	583	0.29	29.24	1.96	0.19	24.1 ± 1.1	26.6 ± 1.2	91	11.26	2.08
FK638	40	3562	0.12	86.24	1.94	0.26	17.9 ± 0.3	21.3 ± 0.4	163	11.04	2.02
FK639b	43	1019	0.39	103.54	1.31	0.12	15.3 ± 0.5	18.0 ± 0.7	208	11.32	1.92
FK640	47	737	0.26	30.82	1.64	0.95	23.5 ± 0.9	26.2 ± 0.9	79	11.57	1.99
FK641	35	707	0.30	36.87	1.54	0.08	29.1 ± 1.3	31.0 ± 1.5	79	10.61	2.29
SG-1	42	711	0.27	28.30	1.64	0.03	29.6 ± 1.2	33.1 ± 1.6	44	11.38	2.38

Table 2. *Cont.*

Sample Number	No. of Grains	N_s	ρ_s (10^5 cm^{-2})	^{238}U (μg/g)	Dpar (μm)	P(χ2)	Pooled Age (Ma ± 1σ)	Central Age (Ma ± 1σ)	N_L	MTL (μm)	SD (μm)
SG-2	14	168	0.22	17.71	1.98	0.40	16.9 ± 3.2	30.0 ± 5.4	5	11.03	2.93
SG-3	13	181	0.15	20.31	1.96	0.87	17.7 ± 2.8	22.8 ± 3.4	20	11.27	2.41
Durango	39	2036	1.97	12.90		0.98	28.9 ± 1.29	29.3 ± 1.3			

3.3. U-Th/He Dating

We analyzed seven AHe samples and seven ZHe samples comprising 40 grains (22 apatite and 18 zircon grains). The apparent AHe ages of all the grains are significantly younger than either the formation or metamorphism ages, indicating a full reset of the AHe system. FK637 has a high intrasample dispersion, with ages between 15.5 ± 9.1 and 56.8 ± 23.5 Ma and with a low eU ranging from 34.9 to 47.5 (Table 3). The eU–age and equivalent spherical radius (ESR)–age diagrams show no correlation (Supplementary File S1, Figure S7). These types of samples may indicate rapid cooling, and the youngest AHe age may reflect a time of fast cooling [60]. The single grain AHe ages of FK638 range from 16.2 ± 1.3 to 26.0 ± 5.0 Ma (Table 3). The eU–age and ESR–age diagrams show a positive correlation (Supplementary File S1, Figure S7), and the mean age of the sample is 21.1 ± 4.9 Ma. The single grain AHe ages of FK639b range from 14.9 ± 25.3 to 22.1 ± 2.6 Ma (Table 3). We neglect the youngest age, which has a high error. The eU–age and ESR–age diagrams show a positive correlation (Supplementary File S1, Figure S3), and the mean age of the sample is 19.9 ± 2.2 Ma. FK640 has low intrasample dispersion and has single grain ages of 20.7 ± 11.6, 23.4 ± 10.4, and 26.7 ± 12.5 Ma, respectively. The eU–age and ESR–age diagrams show a positive correlation (Supplementary File S1, Figure S7), and the mean age of the sample is 23.6 ± 2.5 Ma. FK641 is similar to FK640 and shows low intragrain dispersion. The single grain ages are 15.6 ± 5.3, 14.7 ± 6.7, and 14.3 ± 1.3 Ma, respectively. The eU–age diagram shows a positive correlation, whereas the ESR–age diagram shows no correlation (Supplementary File S1, Figure S7), and the mean age of the sample is 14.9 ± 0.5 Ma (Table 3). We could not measure the apatite crystals for SG1; however, SG2 has low intrasample dispersion and has single grain ages of 16.3 ± 0.3, 10.5 ± 0.6, and 15.5 ± 0.8 Ma (Table 3). The eU–age diagram shows a positive correlation, whereas the ESR–age diagram shows no correlation (Supplementary File S1, Figure S7), and the mean age of the sample is 14.1 ± 2.5 Ma (Table 3). SG3 was collected at the lowest altitude and has the youngest single grain AHe ages, ranging from 4.3 ± 1.0 to 11.9 ± 3.1 Ma (Table 3). The eU–age and ESR–age diagrams show no correlation (Supplementary File S1, Figure S7) and, as mentioned, the youngest single grain age (4.3 ± 1.0 Ma) may reflect a cooling age.

The single grain ZHe ages of FK637 show low dispersion and are significantly younger than the metamorphic zircon ages, but Hozatlıoğlu, Bozkaya, and Yalçın [39] found similar biotite and muscovite Ar-Ar ages from the same unit. The single grain ages are 37.1 ± 0.3, 38.4 ± 0.9, and 38.1 ± 0.4 Ma, with a mean age of 37.9 ± 0.6 Ma (Table 3). The eU–age and ESR–age diagrams show no correlation (Supplementary File S1, Figure S8). Only two zircon grains were analyzed from FK638, yielding ages of 30.4 ± 0.6 and 153.8 ± 16.6 Ma, respectively. The younger ZHe age was used as the ZHe cooling age, and the older ZHe age was neglected, as its age is much older than the metamorphism age (Table 3). The single grain ZHe ages of FK640 show high dispersion, yielding 30.4 ± 0.6, 59.8 ± 0.5, and 142.3 ± 13.2 Ma, respectively. The eU–age and ESR–age diagrams show no correlation (Supplementary File S1, Figure S8), indicating a fast cooling. Similar to FK638, the youngest age was used as the ZHe cooling age. Two zircon grains from FK641 were measured, yielding 44.7 ± 0.8 and 40.7 ± 1.8 Ma, respectively (Table 3). The sample has a mean ZHe age of 42.7 ± 2.0 Ma. SG1 has a high intrasample ZHe age dispersion, yielding 51.2 ± 0.7, 81.7 ± 1.0, and 209.1 ± 6.5 Ma, respectively. The eU–age and ESR–age diagrams correlate negatively (Supplementary File S1, Figure S8), indicating fast cooling, and the youngest ZHE age was used as the cooling time. SG2 yields ZHe ages of 40.5 ± 0.4,

45.3 ± 0.4, and 68.1 ± 0.5 Ma, respectively. The eU–age and the ESR–age diagrams show a positive correlation (Supplementary File S1, Figure S8). The oldest ZHe age is similar to the metamorphism age found in this study, and the two younger ZHe ages are interpreted as cooling ages, with a mean age of 42.9 ± 2.4 Ma (Table 3). Two zircon grains were analyzed from SG3, and only one yielded a meaningful ZHe age of 32.5 ± 0.7 Ma (Table 3).

Table 3. Summary of apatite (U-Th)/He data for metamorphic rocks. [a] FT: alpha-ejection correction after Farley, Wolf, and Silver [52]; [b] eU: effective uranium concentration (U ppm + 0.235 Th ppm); [c] ESR: equivalent spherical radius. Ages and uncertainties in bold text denote weighted mean values. Note that some grains are not included in mean value calculations.

Sample Number	4He (nmol)	Mass (μg)	[a] FT	U (ppm)	Th (ppm)	Sm (ppm)	Th/U	[b] eU (ppm)	Uncorr. Age (Ma)	Corr. Age (Ma)	±1σ (Ma)	[c] ESR (μm)
Apatite												
FK-637-1	6.45×10^{-4}	27.21	0.757	32.51	27.27	35.97	0.85	38.7	11.8	15.5	9.1	50.9
FK-637-3	9.28×10^{-4}	33.38	0.745	33.25	8.09	29.94	0.25	34.9	15.2	20.4	3.7	55.6
FK-637-2	3.03×10^{-3}	29.07	0.731	47.42	1.64	34.88	0.03	47.5	41.5	56.8	23.5	52.4
										18.0	**2.4**	
FK-638-1	1.28×10^{-3}	15.55	0.68	115.61	0.49	44.02	0.00	114.9	13.6	19.9	31.0	44.2
FK-638-2	4.88×10^{-3}	24.33	0.718	199.78	3.45	57.02	0.02	199.1	18.7	26.0	5.0	50.8
FK-638-3	4.71×10^{-4}	12.48	0.66	63.81	21.43	51.33	0.34	68.4	10.7	16.2	1.3	41.4
										21.1	**4.9**	
FK-639B-1	3.86×10^{-4}	19.00	0.696	29.68	12.85	34.77	0.44	32.5	12.3	17.7	3.2	46.1
FK-639B-2	3.98×10^{-4}	6.18	0.571	146.75	1.12	46.71	0.01	145.9	8.5	14.9	25.3	31.5
FK-639B-3	2.60×10^{-3}	13.11	0.653	255.40	11.65	46.88	0.05	256.3	14.4	22.1	2.6	40.0
										19.9	**2.2**	
FK-640-1	1.93×10^{-3}	44.35	0.749	41.20	0.59	23.89	0.01	41.0	20.0	26.7	12.5	56.9
FK-640-2	6.07×10^{-4}	13.61	0.647	50.74	59.83	31.61	1.19	64.4	13.4	20.7	11.6	39.3
FK-640-3	7.26×10^{-4}	17.66	0.674	49.58	4.97	29.95	0.10	50.4	15.8	23.4	10.4	42.8
										23.6	**2.5**	
FK-641-1	8.27×10^{-4}	17.23	0.685	85.18	2.61	41.64	0.03	85.2	10.7	15.6	5.3	45.0
FK-641-2	1.30×10^{-3}	36.75	0.75	60.53	0.75	32.98	0.01	60.3	11.0	14.7	6.7	56.7
FK-641-3	3.53×10^{-4}	19.12	0.687	33.78	13.95	27.66	0.42	36.8	9.8	14.3	1.3	44.6
										14.9	**0.5**	
SG-2-1	6.14×10^{-4}	16.74	0.687	52.37	46.44	12.14	0.89	62.9	11.2	16.3	0.3	45.3
SG-2-2	5.66×10^{-5}	27.23	0.719	5.12	6.36	3.78	1.25	6.6	7.6	10.5	0.6	50.3
SG-2-3	3.13×10^{-4}	15.70	0.675	35.06	12.02	17.76	0.35	37.6	10.5	15.5	0.8	42.9
										14.1	**2.5**	
SG-3-1	3.50×10^{-5}	9.38	0.626	19.78	28.33	4.23	1.44	26.3	3.1	5.0	0.3	37.4
SG-3-2	4.31×10^{-4}	24.96	0.73	43.75	37.10	9.92	0.85	52.1	6.3	8.6	3.3	52.9
SG-3-3	9.47×10^{-5}	13.66	0.646	46.66	12.51	7.53	0.27	49.2	2.8	4.3	1.0	39.1
SG-3-4	1.60×10^{-4}	14.90	0.664	27.14	4.36	4.09	0.16	27.9	7.9	11.9	3.1	42.1
										6.0	**1.9**	
Zircon												
FKZ-637-1	1.14×10^{-2}	27.21	0.757	239.54	164.99	0.97	0.69	276.6	28.1	37.1	0.3	37.6
FKZ-637-2	1.05×10^{-2}	29.07	0.731	228.76	44.40	0.72	0.20	237.5	28.1	38.4	0.9	37.5
FKZ-637-3	1.87×10^{-2}	33.38	0.745	343.01	98.24	1.03	0.29	363.6	28.4	38.1	0.4	41.5
										37.9	**0.6**	
FKZ-638-1	1.23×10^{-2}	15.55	0.68	697.61	66.31	2.34	0.10	708.1	20.7	30.4	0.6	31.8
FKZ-638-2	1.02×10^{-3}	24.33	0.718	6.94	7.44	1.09	1.08	8.6	110.4	153.8	16.6	37.5
FKZ-640-1	1.38×10^{-2}	44.35	0.749	250.81	17.98	0.37	0.07	253.2	22.7	30.4	0.6	60.8
FKZ-640-2	1.35×10^{-2}	13.61	0.647	418.68	251.72	1.61	0.61	474.8	38.7	59.8	0.5	41.5
FKZ-640-3	1.16×10^{-3}	17.66	0.674	12.61	10.21	4.17	0.82	14.9	95.9	142.3	13.2	44.9
										45.1	**14.7**	
FKZ-641-1	1.21×10^{-2}	17.23	0.685	413.64	56.13	1.38	0.14	423.8	30.6	44.7	0.8	47.6

Table 3. *Cont.*

Sample Number	4He (nmol)	Mass (μg)	[a] FT	U (ppm)	Th (ppm)	Sm (ppm)	Th/U	[b] eU (ppm)	Uncorr. Age (Ma)	Corr. Age (Ma)	±1σ (Ma)	[c] ESR (μm)
FKZ-641-2	5.82×10^{-2}	36.75	0.75	956.96	26.67	0.55	0.03	956.2	30.5	40.7	1.8	54.9
										42.7	**2.0**	
SGZ-1-1	6.08×10^{-2}	18.84	0.751	1519.39	158.67	0.68	0.11	1545.6	38.4	51.2	0.7	45.7
SGZ-1-2	6.08×10^{-2}	17.11	0.738	1039.36	216.72	1.09	0.21	1082.7	60.3	81.7	1.0	43.1
SGZ-1-3	6.08×10^{-2}	9.70	0.695	764.81	128.30	2.41	0.17	789.4	145.3	209.1	6.5	36.8
										66.5	**15.3**	
SGZ-2-1	6.08×10^{-2}	53.02	0.821	615.98	98.11	0.45	0.16	634.5	33.3	40.5	0.4	64.4
SGZ-2-3	3.32×10^{-2}	16.44	0.731	988.08	610.67	1.74	0.62	1124.4	33.1	45.3	0.4	36.2
SGZ-2-2	6.08×10^{-2}	11.02	0.692	1922.78	1047.15	2.87	0.55	2154.8	47.1	68.1	0.5	41.8
										42.9	**2.4**	
SGZ-3-1	-5.63×10^{-6}	5.54	0.639	9.02	24.25	5.23	2.73	14.6	−2.6	−4.1	−1.7	30.6
SGZ-3-2	2.41×10^{-2}	14.69	0.732	1258.40	100.58	2.33	0.08	1272.8	23.8	32.5	0.7	42.2

Overall, the samples show a decrease in age from a high closure temperature (ZHe) to low temperature (AHe), showing a single-phase cooling from the Eocene to the late Miocene (Tables 2–4). The age–elevation profiles of SG1, SG2, and SG3 prove the same hypothesis, and either the AHe, AFT, and ZHe ages or the altitude changes indicate a slow cooling from the Eocene to the late Miocene in the region (Figure 5).

Table 4. Summary table of LTT data.

Sample	Altitude (m)	AHe Age ± 1σ (Ma)	AFT Age ± 1σ (Ma)	ZHe Age ± 1σ (Ma)
FK637	1180	18 ± 2.4	26.7 ± 1.6	37.9 ± 0.6
FK638	1181	21.1 ± 4.9	20.4 ± 1.3	30.4 ± 0.6
FK639b	1180	19.9 ± 2.2	18.1 ± 0.9	
FK640	1185	23.6 ± 2.5	25.8 ± 0.9	30.4 ± 0.6
FK641	1157	14.9 ± 0.5	31 ± 1.5	42.7 ± 2
SG1	1275		33.1 ± 1.6	51.2 ± 0.7
SG2	1185	14.1 ± 2.5	32.3 ± 9.9	42.9 ± 2.4
SG3	1130	6 ± 1.9	23.4 ± 4.9	32.5 ± 0.7

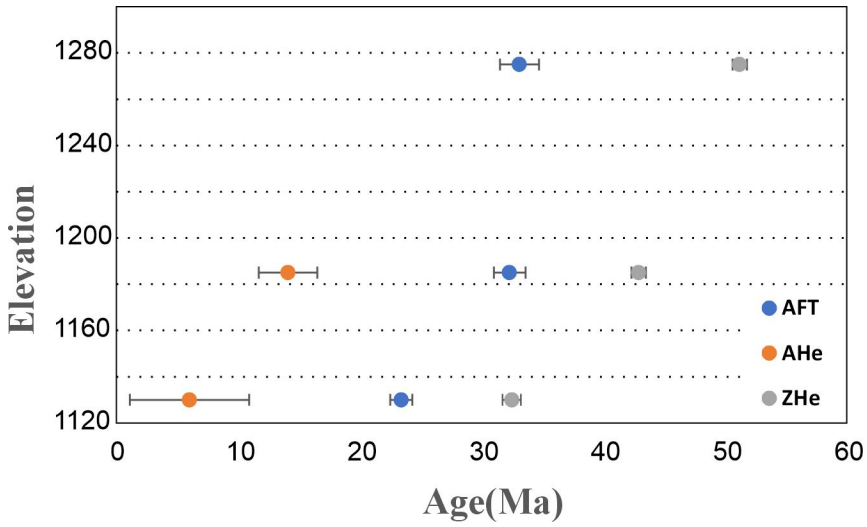

Figure 5. Age–elevation profile of SG1, SG2, and SG3.

3.4. Thermal History Modeling

The thermal history modeling of all the samples shows that they cooled below the Partial Annealing Zone (PAZ) during the Eocene, except for FK639a and FK640; these samples cooled below the PAZ during the Oligocene. All the samples stayed in the PAZ until the middle–late Miocene and left the PAZ during this period (Figure 6). QTQt produces four different models, and mostly, the expected models are used to show the cooling profiles; however, in such cases other models, such as the maximum likelihood, maximum posterior, and maximum mode models, may be more useful to depict the cooling profiles. The expected model shows the weighted mean time–temperature path, the maximum likelihood model shows the best predicted thermal histories, the maximum posterior model shows the maximum probability of the thermal history, and the maximum mode model shows the maximum peak of the probability distribution. Here, we choose the expected mode models, which show the weighted mean time–temperature path of the thermal models (Figure 6).

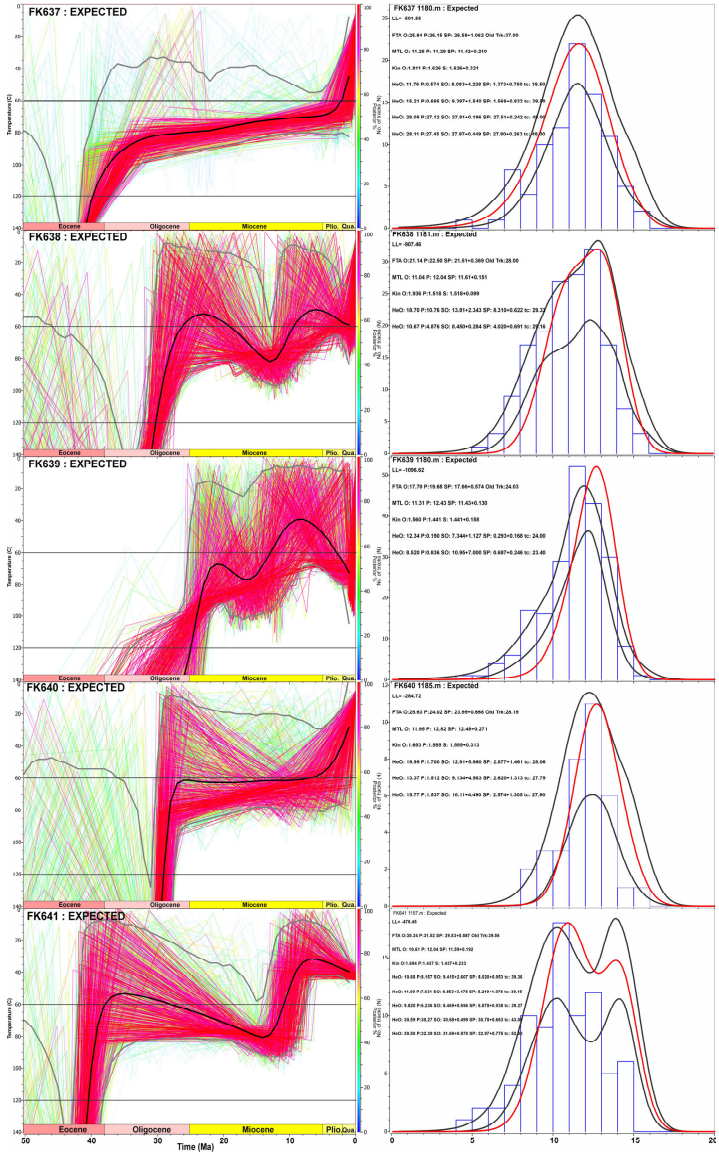

Figure 6. Thermal history modeling results of Yoncayolu formations samples. Here, expected models and TL distributions are shown. The 60 °C and 120 °C lines define the upper and lower boundary of the Partial Annealing Zone, respectively.

Two samples (FK637 and FK641) cooled to above the lower limit (120 °C) of the Partial Annealing Zone (PAZ) during the middle–late Eocene (42–39 Ma). FK637 cooled to 90–80 °C during this period and stayed within the PAZ until Plio–Quaternary in an almost steady-state cooling regime. However, FK641 cooled very fast, left the PAZ during the same period, and then heated to ~80 °C until 16–80 Ma, following a fast-cooling event during the middle–late Miocene (12–8 Ma) (Figure 6).

The samples FK638, FK639, and FK640 passed the PAZ and cooled to the upper margin (60 °C) of the PAZ during the late Oligocene (Figure 6). The samples resided at this temperature and cooled above the PAZ during the middle–late Miocene (Figure 6).

4. Discussion

As a result of the convergence of the Eurasian and Arabian platforms, the 2400 km long Bitlis–Zagros thrust zone formed and is still growing due to the active northward movement of the Arabian platform [61,62]. Due to this convergence, the Eastern Anatolian region has hosted two distinct collision events since the Cretaceous. The first continental collision along the Southeastern Anatolian Orogenic Belt (SAOB) occurred during the late Cretaceous. This collision involved the Eastern Taurides to the north and the Bitlis–Pütürge–Engizek (BPE) metamorphics to the south, following the consumption of the Berit Ocean. This tectonic environment produced several geological features, including an SSZ-type oceanic crust; late-Cretaceous arc-related magmatic, mélange formations; and a late-Cretaceous subduction-related metamorphism on the BPE [1,2,14,63–65]. However, Yılmaz [10] split the BPE from the Malatya–Keban–Binboğa metamorphic massifs within the Nappe Zone located at the lower Nappe, whereas other researchers have interpreted the BPE as a micro-continent located between the Anatolide–Tauride and Arabian platforms. This interpretation is based on the existence of unmetamorphosed equivalents of the BPE on the Arabian platform, suggesting that the BPE represents the northern margin of the rifted Arabian plate and is situated at the southern edge of the short-lived Berit Ocean [3,4,11].

The first record of the exhumation of the BPE, following the continental collision and slab break-off, was determined to be ~60 Ma through the Zircon U-Th/He method applied to samples taken from the BPE [15,66] (Figure 7). Similar-aged non-metamorphic dikes that intruded into the Pütürge metamorphics also confirm the exhumation of the BPE around 60 Ma [67,68].

The ongoing convergence of the Arabian and Anatolide–Tauride platforms has resulted in a second subduction/collision system with various tectonic settings. These settings are associated with the subduction of the oceanic crust north of the main Arabian plate and the subsequent continental collision. This process can be understood by examining the different regions from north to south, delineated by time slices marked by regional unconformities/changes in the depositional settings of sedimentary basins, the development of arc-related magmatism, and changes in deformational styles. The late Cretaceous–Paleocene period was marked by the development of a subduction system in the southern, active Eurasian margin. This process was marked by the deposition of ophiolitic blocks bearing the Kastel Formation, which also served as a décollement surface for the thrusts in the imbrication zone [63,69]. The growth of the imbrication zone in the south and the simultaneous development of arc-related magmatism on the overriding Eurasian plate indicate that the subduction setting began not much earlier than the late Cretaceous in this convergence system [11]. The development of arc magmatism in the overriding plate was interrupted between the middle–late Eocene and Oligocene periods. This interruption and the subsequent re-initiation of magmatism can be explained by the subduction of a mid-ocean ridge [33,69] along the subduction zone [16,70]. Before the ridge subduction, the angle of the subducted plate increased, leading to the development of an extensional setting in the north. In contrast, during and after the ridge subduction, the angle of the slab rapidly decreased, resulting in a regional compressional setting and the interruption of arc magmatism. Within this tectonic framework, both extensional and compressional tectonics controlled the vertical movements of the over-riding plate [11,15].

Extensional tectonics manifest as depressions in a region, forming extensional back-arc or fore-arc basins. The location of arc magmatism defines the boundary between fore-arc and back-arc regions. In this context, the study area lies in the arc-massif part of the fore-arc region [71,72].

However, thermal models of the study area do not show any exhumation/uplift records before the middle Eocene, which might be defined as an extensional period. On the other hand, all the uplift and exhumation events are younger than the middle Eocene. The presence of unmetamorphosed Paleocene dikes in the region [67,73], and the post–middle Eocene uplift of dike-hosting metamorphics, suggest a thermal resetting of the sample points before the middle Eocene and uplift/exhumation during a compressional setting, which is still active in the region. Although the t-T models of some samples (FK638 and FK641) show some partial burial after the main uplift event (Figure 6), the general trend indicates younger uplift ages towards the south. This burial might be related to sediment deposition during fore-arc and later foreland settings or nappe stacking towards the south. Some samples may not have recorded this burial due to their positions relative to the basin margin; they likely were close to the basin margins where the sediment thickness was insufficient to bury them to the temperatures detectable by low-temperature thermochronology, or they were not affected by nappe stacking due to their positions (Figure 7, Supplementary File S3). Aside from these general comments, an evaluation considering the stratigraphic positions of the sample points (Figure 2) and the ZHe, AFT, and AHe ages obtained from each sample point shows that, except for the SG3 and FK641 samples, the ZHe and AFT ages of the sample points increase as expected, stratigraphically upwards. The SG3 sample point is very close to a thrust fault, suggesting that this point could be influenced by the fault zone and exhibit outlier characteristics. The FK641 sample, on the other hand, is located separately from all the other sample point clusters, and the possibility of it being in a different structural block due to a currently unobservable fault may cause this sample to show outlier characteristics. Although these two samples show different characteristics, the ZHe and AFT ages that are consistent with their stratigraphic positions indicate that the sample points have been slowly uplifted in a regionally rising area between approximately 52 Ma (the oldest ZHe age) and approximately 18 Ma (the youngest AFT age). This slow and long-lived regional uplift could be explained by the tectonic block containing the sample points moving southward as a nappe during the ocean closure to the south, with its vertical movement being much slower than its horizontal movement, as expected in nappe movements. On the other hand, the AHe ages obtained from the sample points are inconsistent with their stratigraphic positions. However, when the AHe ages are examined, considering the geographical distribution of the sample points, it is observed that the ages decrease towards the south. This indicates that the sample points were uplifted between approximately 20 Ma and 6 Ma due to local structural elements rather than a regional trend, resulting in younger ages towards the south. This southward, younger aging trend aligns with the direction of thrust propagation in a northerly subduction setting. The thrust propagation onset age of 20 Ma identified in this study closely matches the widely accepted age of the continental collision between the Arabian platform and Eurasia by numerous studies [7,10,18,20,26].

Similarly, the LTT ages along the SAOB (Supplementary File S3, Figure 7) become younger towards the south, which may also be explained by thrust propagation direction. In addition, all the modeling results using the LTT data suggest an Eocene and middle–late Miocene fast uplift of the region, which can be tested by other methods, such as tectonic, paleomagnetism, and sedimentology studies [7,10,20,24,26]. However, the distribution of the LTT ages of the SAOB and their correlation does not show clear evidence for the timing of the subduction-to-continental-collision transition, due to insufficient LTT data for the region to differentiate between the uplift/exhumation trends of different tectonic settings in the time slices. To determine where and during which periods this cooling is related to compression and/or extension, a systematic LTT study of the region is needed. Such a study would help to better understand the transition timing between subduction

and continental collision. It would also clarify their influences on uplift and exhumation trends at the upper-crustal level in different settings within a regional-scale subduction and collision system.

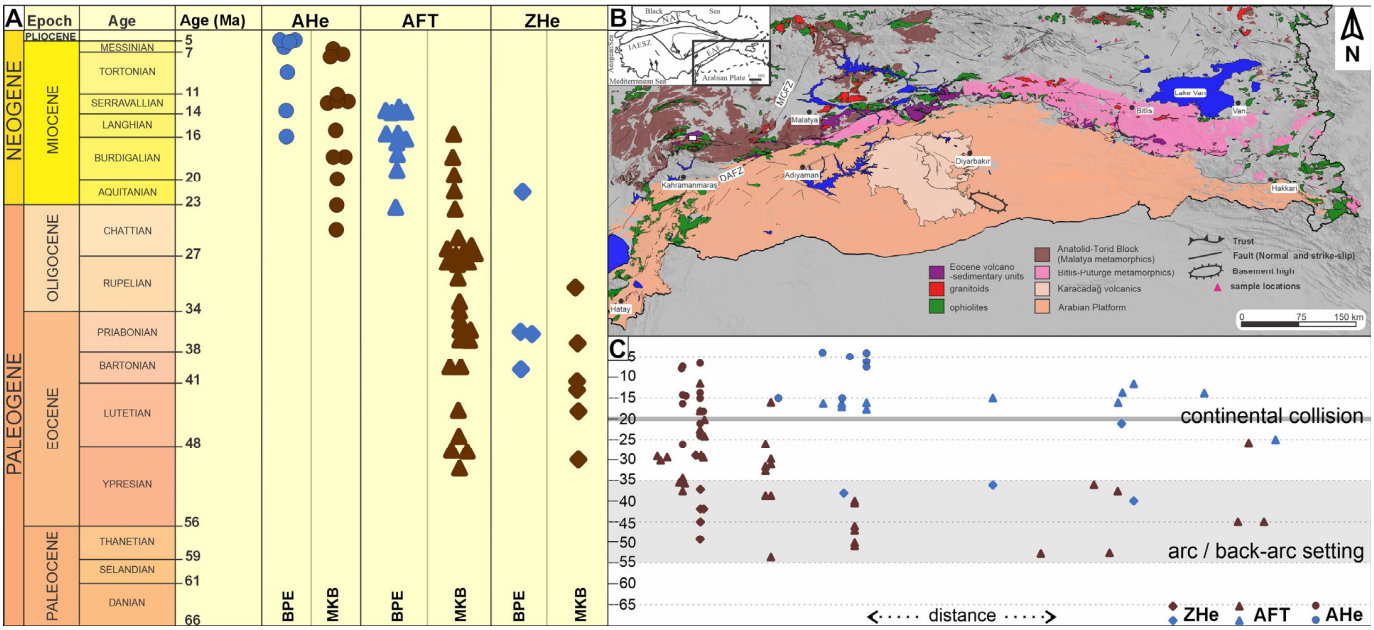

Figure 7. LTT data obtained along the Southeast Anatolian Orogenic Belt. (**A**) LTT data are shown in the Geological Time Scale [74], clustered into two groups. BPE: Bitlis–Pütürge–Engizek metamorphics; MKB: Malatya–Keban–Binboğa metamorphics. (**B**,**C**) Distribution of LTT data along the Southeast Anatolian Orogenic Belt both on the map and age–distance graph [18,75–83]. LTT data from Okay, Zattin, and Cavazza [7]; Karaoğlan, Parlak, Hejl, Neubauer, and Klötzli [11]; Cavazza, Cattò, Zattin, Okay, and Reiners [15]; Topak [25]; Whitney, Delph, Thomson, Beck, Brocard, Cosca, Darin, Kaymakcı, Meijers, Okay, Rojay, Teyssier, and Umhoefer [34], and this study. Note that in (**C**), the horizontal axis has the same distance scale as in (**B**).

5. Conclusions

The LTT data obtained from the Nappe Zone along the SAOB suggest that the exhumation of the active margin was initiated during the Eocene. The Eocene epoch was identified as the arc–back-arc setting in the region. The extensional regime in the region led to tectonic denudation, and the magmatic/metamorphic rocks were exhumed first in the northern and then in the southern part of the Nappe Zone of the SAOB. The region continued its uplifting through the Oligocene during the growth of an accretionary prism and, finally, the Miocene continental collision occurred without changing the uplift regime recorded by LTT. The continental shortening and development of the mountain chain (Eastern Taurides) did not affect the region dramatically. Hence, the LTT data record a slow but continuous uplift. The LTT data show fingerprints of thrust propagation from north to south. Overall, the current state of the LTT data suggest more systematic studies are needed to enlighten the timing of the transition between subduction and continental collision and mountain-building processes along the SAOB.

Supplementary Materials: The following supporting information can be downloaded at https://www.mdpi.com/article/10.3390/min14060614/s1. Figure S1: Thin sections of the samples collected from the Yoncayolu formation; Figure S2: Zircon cathodoluminescence images for sample FK637; Figure S3: Zircon cathodoluminescence images for sample FK640; Figure S4: Zircon cathodoluminescence images for sample FK641; Figure S5: Zircon cathodoluminescence images for sample SG2; Figure S6: The radial plots of the AFT analyses; Figure S7: The eU–age and ESR–age diagrams for the AHe analyses of the samples from the Yoncayolu Formation; Figure S8: The eU–age and ESR–age diagrams of the ZHe analyses of the samples from the Yoncayolu Formation; Supplementary

File 2 Table S1: LA-ICP-MS Zircon U-Pb data; Google Earth File, S1: The geographic locations of the LTT data the along Southeast Anatolian Orogenic Belt.

Author Contributions: Conceptualization, S.G. and F.K.; writing—original draft preparation, F.K., E.G., and S.G.; methodology, F.K., S.G. and E.G.; formal analysis, S.G.; software, S.G.; supervision, F.K.; project administration, F.K.; funding acquisition, F.K. All authors have read and agreed to the published version of the manuscript.

Funding: This research was funded by the Cukurova University Scientific Research Projects Office, grant number FYL-2022-14181, and the APC was funded by F.K.

Data Availability Statement: Datasets for this research are included in this paper (and its Supplementary Materials). [Creative Commons Attribution License].

Acknowledgments: This study was the first author's MSc thesis. The first author (S.G.) acknowledges the TUBİTAK-ARDEB projects 118Y386 and 121Y357 for scholarships during their MSc program. F.K. was supported by institutional support from the Institute of Geology of the Czech Academy of Sciences (project No. RVO67985831). The authors acknowledge the comments and contributions of two anonymous reviewers.

Conflicts of Interest: The authors declare no conflicts of interest.

References

1. Oberhänsli, R.; Bousquet, R.; Candan, O.; Okay, A. Dating Subduction Events in East Anatolia, Turkey. *Turk. J. Earth Sci.* **2012**, *21*, 1–17.
2. Oberhänsli, R.; Candan, O.; Bousquet, R.; Rimmele, G.; Okay, A.; Goff, J. Alpine high pressure evolution of the eastern Bitlis complex, SE Turkey. In *Sedimentary Basin Tectonics from the Black Sea and Caucasus to the Arabian Platform*; Sosson, M., Kaymakci, N., Stephenson, R.A., Bergerat, F., Starostenko, V., Eds.; Special Publications; Geological Society: London, UK, 2010; Volume 340, pp. 461–483.
3. Robertson, A.H.F.; Parlak, O.; Taslı, K. Testing alternative tectonic models for the Permian-Pleistocene tectonic development of the Kyrenia Range, N Cyprus: Implications for E Mediterranean Tethyan palaeogeography. *Gondwana Res.* **2024**, *132*, 343–379. [CrossRef]
4. Robertson, A.H.F.; Parlak, O.; Ustaomer, T. Overview of the Palaeozoic-neogene evolution of neotethys in the Eastern Mediterranean region (Southern Turkey, Cyprus, Syria). *Pet. Geosci.* **2012**, *18*, 381–404. [CrossRef]
5. Garfunkel, Z. Neotethyan ophiolites: Formation and obduction within the life cycle of the host basins. In *Tectonic Development of the Eastern Mediterranean Region*; Robertson, A.H.F., Mountrakis, D., Eds.; Special Publications; Geological Society: London, UK, 2006; Volume 260, pp. 301–326.
6. Garfunkel, Z. Origin of the Eastern Mediterranean basin: A reevaluation. *Tectonophysics* **2004**, *391*, 11–34. [CrossRef]
7. Okay, A.I.; Zattin, M.; Cavazza, W. Apatite fission-track data for the Miocene Arabia-Eurasia collision. *Geology* **2010**, *38*, 35–38. [CrossRef]
8. Parlak, O.; Rizaoglu, T.; Bagci, U.; Karaoglan, F.; Hock, V. Tectonic significance of the geochemistry and petrology of ophiolites in southeast Anatolia, Turkey. *Tectonophysics* **2009**, *473*, 173–187. [CrossRef]
9. Allen, M.B.; Armstrong, H.A. Arabia-Eurasia collision and the forcing of mid-Cenozoic global cooling. *Palaeogeogr. Palaeoclimatol. Palaeoecol.* **2008**, *265*, 52–58. [CrossRef]
10. Yılmaz, Y. Southeast Anatolian Orogenic Belt revisited (geology and evolution). *Can. J. Earth Sci.* **2019**, *56*, 1163–1180. [CrossRef]
11. Karaoğlan, F.; Parlak, O.; Hejl, E.; Neubauer, F.; Klötzli, U. The temporal evolution of the active margin along the Southeast Anatolian Orogenic Belt (SE Turkey): Evidence from U–Pb, Ar–Ar and fission track chronology. *Gondwana Res.* **2016**, *33*, 190–208. [CrossRef]
12. Yılmaz, Y.; Yiğitbaş, E.; Çemen, İ. Tectonics of the Southeast Anatolian Orogenic Belt. In *Compressional Tectonics*; John Wiley & Sons: Hoboken, NJ, USA, 2023; pp. 203–222.
13. Rolland, Y.; Perincek, D.; Kaymakci, N.; Sosson, M.; Barrier, E.; Avagyan, A. Evidence for ~80–75Ma subduction jump during Anatolide–Tauride–Armenian block accretion and ~48 Ma Arabia–Eurasia collision in Lesser Caucasus–East Anatolia. *J. Geodyn.* **2012**, *56–57*, 76–85. [CrossRef]
14. Oberhänsli, R.; Koralay, E.; Candan, O.; Pourteau, A.; Bousquet, R. Late Cretaceous eclogitic high-pressure relics in the Bitlis Massif. *Geodin. Acta* **2014**, *26*, 175–190. [CrossRef]
15. Cavazza, W.; Cattò, S.; Zattin, M.; Okay, A.I.; Reiners, P. Thermochronology of the Miocene Arabia-Eurasia collision zone of southeastern Turkey. *Geosphere* **2018**, *14*, 2277–2293. [CrossRef]
16. Karaoğlan, F.; Parlak, O.; Robertson, A.; Thöni, M.; Klötzli, U.; Koller, F.; Okay, A.İ. Evidence of Eocene high-temperature/high-pressure metamorphism of ophiolitic rocks and granitoid intrusion related to Neotethyan subduction processes (Doğanşehir area, SE Anatolia). In *Geological Development of Anatolia and the Easternmost Mediterranean Region*; Robertson, A.H.F., Parlak, O., Ünlügenç, U.C., Eds.; Special Publications; Geological Society: London, UK, 2013; Volume 372, pp. 249–272.

17. Aktaş, G.; Robertson, A.H.F. The Maden Complex, SE Turkey: Evolution of a Neotethyan active margin. In *The Geological Evolution of the Eastern Mediterranean*; Dixon, J.E., Robertson, A.H.F., Fleet, A.J., Eds.; Special Publications; Geological Society: London, UK, 1984; Volume 17, pp. 375–402.
18. Yılmaz, Y. New Evidence and Model on the Evolution of the Southeast Anatolian Orogen. *Geol. Soc. Am. Bull.* **1993**, *105*, 251–271. [CrossRef]
19. Yiğitbaş, E.; Yılmaz, Y. New evidence and solution to the Maden complex controversy of the Southeast Anatolian orogenic belt (Turkey). *Geol. Rundsch.* **1996**, *85*, 250–263. [CrossRef]
20. Bialik, O.M.; Frank, M.; Betzler, C.; Zammit, R.; Waldmann, N.D. Two-step closure of the Miocene Indian Ocean Gateway to the Mediterranean. *Sci. Rep.* **2019**, *9*, 8842. [CrossRef] [PubMed]
21. Harzhauser, M.; Kroh, A.; Mandic, O.; Piller, W.E.; Gohlich, U.; Reuter, M.; Berning, B. Biogeographic responses to geodynamics: A key study all around the Oligo-Miocene Tethyan Seaway. *Zool. Anz.* **2007**, *246*, 241–256. [CrossRef]
22. Hüsing, S.K.; Zachariasse, W.-J.; van Hinsbergen, D.J.J.; Krijgsman, W.; Inceöz, M.; Harzhauser, M.; Mandic, O.; Kroh, A. Oligocene–Miocene basin evolution in SE Anatolia, Turkey: Constraints on the closure of the eastern Tethys gateway. In *Collision and Collapse at the Africa-Arabia-Eurasia Subduction Zone*; Van Hinsbergen, D.J.J., Edwards, M.A., Govers, R., Eds.; Special Publications; Geological Society: London, UK, 2009; Volume 311, pp. 107–132.
23. Şengör, A.M.C.; Özeren, M.S.; Keskin, M.; Sakinç, M.; Özbakır, A.D.; Kayan, İ. Eastern Turkish high plateau as a small Turkic-type orogen: Implications for post-collisional crust-forming processes in Turkic-type orogens. *Earth-Sci. Rev.* **2008**, *90*, 1–48. [CrossRef]
24. Şengör, A.M.C.; Yılmaz, Y. Tethyan Evolution of Turkey—A Plate Tectonic Approach. *Tectonophysics* **1981**, *75*, 181–241. [CrossRef]
25. Topak, Y. Growth of the imbrication zone along the southeast Anatolian orogenic belt: Evidence from fission track thermochronology from Gölbaşı region (SE Turkey). *Turk. J. Earth Sci.* **2022**, *31*, 178–192. [CrossRef]
26. Gülyüz, E.; Durak, H.; Özkaptan, M.; Krijgsman, W. Paleomagnetic constraints on the early Miocene closure of the southern Neo-Tethys (Van region; East Anatolia): Inferences for the timing of Eurasia-Arabia collision. *Glob. Planet. Chang.* **2020**, *185*, 103089. [CrossRef]
27. Bozkurt, E. Neotectonics of Turkey—A synthesis. *Geodin. Acta* **2001**, *14*, 3–30. [CrossRef]
28. Elitok, Ö.; Dolmaz, M.N. Tectonic Escape Mechanism in the Crustal Evolution of Eastern Anatolian Region (Turkey). In *New Frontiers in Tectonic Research—At the Midst of Plate Convergence*; Schattner, U., Ed.; IntechOpen: Rijeka, Croatia, 2011; Chapter 11.
29. Koç, A.; Kaymakçı, N. Kinematics of Surgu Fault Zone (Malatya, Turkey): A remote sensing study. *J. Geodyn.* **2013**, *65*, 292–307. [CrossRef]
30. Westaway, R.; Arger, J. Kinematics of the Malatya-Ovacik fault zone. *Geodin. Acta* **2001**, *14*, 103–131. [CrossRef]
31. Westaway, R.; Demir, T.; Seyrek, A. Geometry of the Turkey-Arabia and Africa-Arabia plate boundaries in the latest Miocene to Mid-Pliocene: The role of the Malatya-Ovacık Fault Zone in eastern Turkey. *eEarth* **2008**, *3*, 27–35. [CrossRef]
32. Westaway, R.; Demir, T.; Seyrek, A.; Beck, A. Kinematics of active left-lateral faulting in SE Turkey from offset Pleistocene river gorges: Improved constraint on the rate and history of relative motion between the Turkish and Arabian plates. *J. Geol. Soc. Lond.* **2006**, *163*, 149–164. [CrossRef]
33. Kaymakci, N.; Inceöz, M.; Ertepinar, P.; Koç, A. *Late Cretaceous to Recent kinematics of SE Anatolia (Turkey)*; Special Publications; Geological Society: London, UK, 2010; Volume 340, pp. 409–435. [CrossRef]
34. Whitney, D.L.; Delph, J.R.; Thomson, S.N.; Beck, S.L.; Brocard, G.Y.; Cosca, M.A.; Darin, M.H.; Kaymakcı, N.; Meijers, M.J.M.; Okay, A.I.; et al. Breaking plates: Creation of the East Anatolian fault, the Anatolian plate, and a tectonic escape system. *Geology* **2023**, *51*, 673–677. [CrossRef]
35. Emre, Ö.; Duman, T.Y.; Özalp, S.; Saroglu, F.; Olgun, S.; Elmaci, H.; Çan, T. Active fault database of Turkey. *Bull. Earthq. Eng.* **2018**, *16*, 3229–3275. [CrossRef]
36. Hisarlı, Z.M.; Çinku, M.; Ustaömer, T.; Keskin, M.; Orbay, N. Neotectonic deformation in the Eurasia–Arabia collision zone, the East Anatolian Plateau, E Turkey: Evidence from palaeomagnetic study of Neogene–Quaternary volcanic rocks. *Int. J. Earth Sci.* **2015**, 1–27. [CrossRef]
37. Li, Y.; Wang, C.; Dai, J.; Xu, G.; Hou, Y.; Li, X. Propagation of the deformation and growth of the Tibetan–Himalayan orogen: A review. *Earth-Sci. Rev.* **2015**, *143*, 36–61. [CrossRef]
38. Yılmaz, Y.; Yiğitbaş, E.; Çemen, İ. Tectonics of the Southeast Anatolian Orogenic Belt. *Earth Space Sci. Open Arch.* **2022**, 1–40. [CrossRef]
39. Hozatlıoğlu, D.; Bozkaya, Ö.; Yalçın, H. Göksun, Afşin ve Ekinözü (Kahramanmaraş, Türkiye) Metamorfitlerindeki Fillosilikatların Jeokimyasal Özellikleri. *Türkiye Jeoloji Bülteni* **2020**, *64*, 41–74. [CrossRef]
40. Yılmaz, A.; Bedi, Y.; Uysal, Ş.; Yusufoğlu, H.; Atabey, E.; ve Aydın, N. Doğu Toroslar'da Uzunyayla ile Beritdağı Arasının jeolojik yapısı. *TPJD Bülteni* **1993**, *5*, 69–87.
41. Bedi, Y.; Yusufoğlu, H.; Beyazpirinç, M.; Özkan, M.K.; Usta, D.; Yıldız, H. *Doğu Toroslar'ın Jeodinamik Evrimi (Afşin-Elbistan-Goksun-Sariz Dolayı) [Geodynaic Evolution of Eattern Taurides (Afşin-Elbitan-Göksun-Sarız)]*; 11150; Maden Tetkik Ve Arama Genel Müdürlüğü: Ankara, Turkey, 2009; p. 388.
42. Hozatlıoğlu, D.; Bozkaya, Ö.; Yalçın, H.; Yılmaz, H. Mineralogical characteristics of metamorphic massif units outcropping in Göksun, Afşin and Ekinözü (Kahramanmaraş) region. *Bull. Miner. Res. Explor.* **2019**, 1–10. [CrossRef]
43. Bilgiç, T. Turkey Geological Map, Sheet Sivas: Ankara, Turkey: Maden Tetkik ve Arama Genel Müdürlüğü, Scale 1:500,000. 2002. Available online: https://www.mta.gov.tr/v3.0/sayfalar/hizmetler/doc/SIVAS.pdf (accessed on 11 June 2024).

44. Günay, Y.; Şenel, M. Turkey Geological Map, Sheet Cizre: Ankara, Turkey: Maden Tetkik ve Arama Genel Müdürlüğü, Scale 1:500,000. 2002. Available online: https://www.mta.gov.tr/v3.0/sayfalar/hizmetler/doc/CIZRE.pdf (accessed on 11 June 2024).
45. Şenel, M.; Ercan, T. Turkey Geological Map, Sheet Van: Ankara, Turkey, Maden Tetkik ve Arama Genel Müdürlüğü, Scale 1:500,000. 2002. Available online: https://www.mta.gov.tr/v3.0/sayfalar/hizmetler/doc/VAN.pdf (accessed on 11 June 2024).
46. Ulu, U. Turkey Geological Map, Sheet Hatay: Ankara, Turkey: Maden Tetkik ve Arama Genel Müdürlüğü, Scale 1:500,000. 2002. Available online: https://www.mta.gov.tr/v3.0/sayfalar/hizmetler/doc/HATAY.pdf (accessed on 11 June 2024).
47. Tarhan, N. Turkey Geological Map, Sheet Erzurum: Ankara, Turkey: Maden Tetkik ve Arama Genel Müdürlüğü, Scale 1:500,000. 2002. Available online: https://www.mta.gov.tr/v3.0/sayfalar/hizmetler/doc/Erzurum.pdf (accessed on 11 June 2024).
48. Bozkurt, E.; Mittwede, S.K. Introduction to the Geology of Turkey—A Synthesis. *Int. Geol. Rev.* **2001**, *43*, 578–594. [CrossRef]
49. Žák, J.; Svojtka, M.; Hajná, J.; Ackerman, L. Detrital zircon geochronology and processes in accretionary wedges. *Earth-Sci. Rev.* **2020**, *207*, 103214. [CrossRef]
50. Gulyuz, E. Apatite fission track dating of the Beypazari Granitoid: Insight for the inception of collision along the Northern Neotethys, Turkey. *Geodin. Acta* **2020**, *32*, 1–10. [CrossRef]
51. Farley, K.A. (U-Th)/He Dating: Techniques, Calibrations, and Applications. *Rev. Mineral. Geochem.* **2002**, *47*, 819–844. [CrossRef]
52. Farley, K.A.; Wolf, R.A.; Silver, L.T. The effects of long alpha-stopping distances on (U-Th)/He ages. *Geochim. Cosmochim. Acta* **1996**, *60*, 4223–4229. [CrossRef]
53. Gallagher, K. Transdimensional inverse thermal history modeling for quantitative thermochronology. *J. Geophys. Res. Solid Earth* **2012**, *117*. [CrossRef]
54. Ketcham, R.A.; Carter, A.; Donelick, R.A.; Barbarand, J.; Hurford, A.J. Improved modeling of fission-track annealing in apatite. *Am. Mineral.* **2007**, *92*, 799–810. [CrossRef]
55. Flowers, R.M.; Ketcham, R.A.; Shuster, D.L.; Farley, K.A. Apatite (U–Th)/He thermochronometry using a radiation damage accumulation and annealing model. *Geochim. Cosmochim. Acta* **2009**, *73*, 2347–2365. [CrossRef]
56. Guenthner, W.R.; Reiners, P.W.; Drake, H.; Tillberg, M. Zircon, titanite, and apatite (U-Th)/He ages and age-eU correlations from the Fennoscandian Shield, southern Sweden. *Tectonics* **2017**, *36*, 1254–1274. [CrossRef]
57. Ketcham, R.A.; Gautheron, C.; Tassan-Got, L. Accounting for long alpha-particle stopping distances in (U-Th-Sm)/He geochronology: Refinement of the baseline case. *Geochim. Cosmochim. Acta* **2011**, *75*, 7779–7791. [CrossRef]
58. Linnemann, U.; Ouzegane, K.; Drareni, A.; Hofmann, M.; Becker, S.; Gärtner, A.; Sagawe, A. Sands of West Gondwana: An archive of secular magmatism and plate interactions—A case study from the Cambro-Ordovician section of the Tassili Ouan Ahaggar (Algerian Sahara) using U–Pb–LA-ICP-MS detrital zircon ages. *Lithos* **2011**, *123*, 188–203. [CrossRef]
59. Vermeesch, P. RadialPlotter: A Java application for fission track, luminescence and other radial plots. *Radiat. Meas.* **2009**, *44*, 409–410. [CrossRef]
60. He, J.; Thomson, S.N.; Reiners, P.W.; Hemming, S.R.; Licht, K.J. Rapid erosion of the central Transantarctic Mountains at the Eocene-Oligocene transition: Evidence from skewed (U-Th)/He date distributions near Beardmore Glacier. *Earth Planet. Sci. Lett.* **2021**, *567*, 117009. [CrossRef]
61. Reilinger, R.; McClusky, S.; Vernant, P.; Lawrence, S.; Ergintav, S.; Cakmak, R.; Ozener, H.; Kadirov, F.; Guliev, I.; Stepanyan, R.; et al. GPS constraints on continental deformation in the Africa-Arabia-Eurasia continental collision zone and implications for the dynamics of plate interactions. *J. Geophys. Res. Solid Earth* **2006**, *111*. [CrossRef]
62. Reilinger, R.E.; McClusky, S.C.; Oral, M.B.; King, R.W.; Toksoz, M.N.; Barka, A.A.; Kinik, I.; Lenk, O.; Sanli, I. Global Positioning System measurements of present-day crustal movements in the Arabia-Africa-Eurasia plate collision zone. *J. Geophys. Res. Solid Earth* **1997**, *102*, 9983–9999. [CrossRef]
63. Ural, M.; Arslan, M.; Göncüoglu, M.C.; Tekin, K.U.; Kürüm, S. Late Cretaceous arc and back-arc formation within the Southern Neotethys: Whole-rock, trace element and Sr-Nd-Pb isotopic data from basaltic rocks of the Yüksekova Complex (Malatya-Elazığ, SE Turkey). *Ofioliti* **2015**, *40*, 57–72.
64. Ural, M.; Sayit, K.; Tekin, U.T. Whole-Rock and Nd-Pb Isotope Geochemistry and Radiolarian Ages of the Volcanics from the Yüksekova Complex (Maden Area, Elaziğ, E Turkey): Implications for A Late Cretaceous (Santonian-Campanian) Back-Arc Basin in the Southern Neotethys. *Ofioliti* **2022**, *47*, 65–83. [CrossRef]
65. Göncüoğlu, C.; Turhan, N. Geology of the Bitlis Metamorphic Belt. In *Geology of the Taurus Belt*; Tekeli, O., Göncüoğlu, M.C., Eds.; Mineral Research and Expolaration Instutute of Turkey (MTA): Ankara, Turkey, 1984; pp. 237–244.
66. Okay, A.I.; Zattin, M.; Özcan, E.; Sunal, G. Uplift of Anatolia. *Turk. J. Earth Sci.* **2020**, *29*, 696–713. [CrossRef]
67. Pişkin, Ö.; Delaloye, M. Petrologie et G eochronologie des ophiolites de Çelikhan (Taurus Oriental, Turquie). *Schweiz. Mineral. Petrogr. Mitteilungen* **1981**, *61*, 133–145.
68. Pişkin, Ö. Çelikhan Doğusu Lökokuvars-monzonitleri Üzerine Petrokimya ve Jeokronoloji Verileri (Adıyaman-Türkiye). *Türkiye Jeoloji Kurumu Bülteni* **1978**, *21*, 107–111.
69. Tuncer, M. Neotethyan Tectonostratigraphic Evolution of SE Anatolian Basin, Türkiye. Ph.D. Thesis, Middle East Technical University, Ankara, Turkey, 2023.
70. Yılmaz, H.; Alpaslan, M.; Temel, A. Two-stage felsic volcanism in the western part of the southeastern Anatolian orogen: Petrologic and geodynamic implications. *Int. Geol. Rev.* **2007**, *49*, 120–141. [CrossRef]
71. Dickinson, W.R.; Seely, D.R. Structure and Stratigraphy of Forearc Regions. *AAPG Bull.* **1979**, *63*, 2–31. [CrossRef]

72. Dickinson, W.R.; Seely, D.R. Forearc Stratigraphy and Structure. In Proceedings of the Offshore Technology Conference, Houston, TX, USA, 2 May 1977.
73. Pişkin, Ö. Çelikhan Çevresi Ultrabazikleri içindeki Rodenjitler ve Kimyasal Analizleri. *Türkiye Jeoloji Kurumu Bülteni* **1975**, *18*, 17–20.
74. Gradstein, F.M.; Ogg, J.G.; Smith, A.G. *A Geologic Time Scale 2004*; Cambridge University Press: Cambridge, UK, 2004.
75. Slama, J.; Kosler, J.; Condon, D.J.; Crowley, J.L.; Gerdes, A.; Hanchar, J.M.; Horstwood, M.S.A.; Morris, G.A.; Nasdala, L.; Norberg, N.; et al. Plesovice zircon - A new natural reference material for U-Pb and Hf isotopic microanalysis. *Chem. Geol.* **2008**, *249*, 1–35. [CrossRef]
76. Jackson, S.E.; Pearson, N.J.; Griffin, W.L.; Belousova, E.A. The application of laser ablation-inductively coupled plasma-mass spectrometry to in situ U–Pb zircon geochronology. *Chem. Geol.* **2004**, *211*, 47–69. [CrossRef]
77. Wiedenbeck, M.; AllÉ, P.; Corfu, F.; Griffin, W.L.; Meier, M.; Oberli, F.; Quadt, A.V.; Roddick, J.C.; Spiegel, W. Three Natural Zircon Standards For U-Th-Pb, Lu-Hf, Trace Element And REE Analyses. *Geostand. Newsl.* **1995**, *19*, 1–23. [CrossRef]
78. Petrus, J.A.; Kamber, B.S. VizualAge: A Novel Approach to Laser Ablation ICP-MS U-Pb Geochronology Data Reduction. *Geostand. Geoanal. Res.* **2012**, *36*, 247–270. [CrossRef]
79. Paton, C.; Hellstrom, J.; Paul, B.; Woodhead, J.; Hergt, J. Iolite: Freeware for the visualisation and processing of mass spectrometric data. *J. Anal. At. Spectrom.* **2011**, *26*, 2508–2518. [CrossRef]
80. Vermeesch, P. IsoplotR: A free and open toolbox for geochronology. *Geosci. Front.* **2018**, *9*, 1479–1493. [CrossRef]
81. Hasebe, N.; Barbarand, J.; Jarvis, K.; Carter, A.; Hurford, A.J. Apatite fission-track chronometry using laser ablation ICP-MS. *Chem. Geol.* **2004**, *207*, 135–145. [CrossRef]
82. Lin, J.; Liu, Y.S.; Yang, Y.H.; Hu, Z.C. Calibration and correction of LA-ICP-MS and LA-MC-ICP-MS analyses for element contents and isotopic ratios. *Solid Earth Sci.* **2016**, *1*, 5–27. [CrossRef]
83. Paton, C.; Woodhead, J.D.; Hellstrom, J.C.; Hergt, J.M.; Greig, A.; Maas, R. Improved laser ablation U-Pb zircon geochronology through robust downhole fractionation correction. *Geochem. Geophys. Geosyst.* **2010**, *11*, Q0AA06. [CrossRef]

Disclaimer/Publisher's Note: The statements, opinions and data contained in all publications are solely those of the individual author(s) and contributor(s) and not of MDPI and/or the editor(s). MDPI and/or the editor(s) disclaim responsibility for any injury to people or property resulting from any ideas, methods, instructions or products referred to in the content.